ACS Photonics

Article

pubs.acs.org/journal/apchd5

All-Dielectric Color Filters Using SiGe-Based Mie Resonator Arrays

Thomas Wood,*[,†,‡] Meher Naffouti,[†,§,∥] Johann Berthelot,[⊥] Thomas David,[†] Jean-Benoît Claude,[†] Léo Métayer,[†] Anne Delobbe,[#] Luc Favre,[†] Antoine Ronda,[†] Isabelle Berbezier,[†] Nicolas Bonod,[⊥] and Marco Abbarchi*[,†]

[†]CNRS, Aix-Marseille Université, Centrale Marseille, IM2NP, UMR 7334, Campus de St. Jérôme, 13397 Marseille, France

[§]Laboratoire de Micro-Optoélectroniques et Nanostructures, Faculté des Sciences de Monastir, Université de Monastir, Monastir 5019, Tunisia

[⊥]Aix-Marseille Univ, CNRS, Centrale Marseille, Institut Fresnel, Marseille, France

[#]Orsay Physics 13710 Fuveau, France

Supporting Information

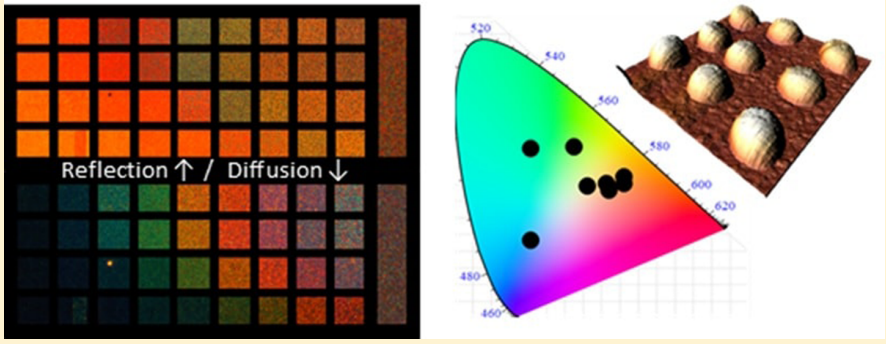

ABSTRACT: Dielectric Mie resonators have attracted a great deal of attention over the past few years thanks to their remarkable capabilities in manipulating light propagation at the nanoscale. However, the practical implementation of technological products is still elusive. One of the important limits is the absence of a high-performing material and a fabrication method that can be easily integrated into modern microelectronic devices at affordable costs. Here, we provide theoretical and experimental evidence of an alternative semiconductor material, SiGe alloys, for dielectric Mie resonator applications. As a material compatible with the processing requirements of the semiconductor industry, it possesses comparable optical properties to its conventional Si-based counterpart at visible frequencies in spite of its higher optical losses. These dielectric resonant particles can be obtained over very large surfaces on arbitrary silica substrates via spontaneous solid state dewetting of ultrathin (<100 nm) SiGe amorphous layers. Furthermore, the polycrystalline SiGe islands can be precisely organized in uniform arrays featuring low size dispersion. As an example, we demonstrate SiGe-based Mie resonator arrays functioning as color pass-band filters across the full visible spectral range. The filters function both in transmission and diffusion and are fabricated using a methodology compatible with C-MOS implemetation.

KEYWORDS: *SiGe alloys, Mie resonator, solid-state dewetting, color-filters, finite difference−time domain simulations, surface functionalization*

Light management using dielectric Mie resonators (MRs),[1] particularly silicon nanoparticles, has been the subject of intense interest in the literature for the past decade.[2−4] This work has led to a host of innovative applications in domains such as sensing and photovoltaics where efficient light trapping is required.[5−8] Of particular note in this area is the substrate-coupling phenomenon, whereby MRs are able to channel optical energy from the ambient toward a bulk material by the extension of the resonantly confined fields into the substrate, as this mechanism forms the crux of the required "trapping" behavior.[9,10] Furthermore, modifying geometric properties of the MRs allows for control over the light−matter interaction, beginning with the well-known interplay between the resonant wavelengths and the size and refractive index of the MRs.[11,12] More complex examples include the coupling of two or more resonators allowing for polarization-sensitive interactions[13,14] and controlling the morphology of the MRs to determine the angular selectivity of the so-formed metasurfaces.[15,16] We note also that due to their low loss at visible and NIR optical frequencies, all-dielectric Mie resonators are fast surpassing plasmonics as the dominant technique for managing light-matter interactions at subwavelength scales.

Received: November 26, 2016
Published: March 13, 2017

DOI: 10.1021/acsphotonics.6b00944
ACS Photonics 2017, 4, 873−883

Over the past decade, during which MRs have been studied intensively from both a theoretical and practical point of view, fabrication methods have been refined to allow for the formation of arrays of precisely sized and positioned resonant particles. Techniques including e-beam lithography coupled with reactive ion etching[17] or chemical etching,[18] ion sputtering,[19] nanoimprinting[20] and laser-based writing[21] and ablation[22] methods have the advantage of producing MR arrays featuring islands with low size dispersions and well-defined positions on their substrates. Another emerging method for the fabrication of MRs is solid state dewetting of monocrystalline SOI[23−26] type structures, consisting of ultrathin (∼10 nm) Si layers on a buried oxide (BOX) layer atop a silicon substrate. This method is suitable for application to large surfaces, at the expense of sacrificing the spatial organization and fine control over the islands' dimensions[27,28] and relative positions. The technique can be refined through the addition of a templating step,[29] whereby narrow (<100 nm) trenches are milled before the dewetting (e.g., by direct etching via focused ion beam, FIB), providing excellent control over the spatial positioning and size distribution of the formed MRs.

So far, silicon has been the material of choice for the implementation of this class of resonant dielectric particles and related meta-surfaces. Other materials of note are gallium phosphide (GaP),[30] aluminum gallium arsenide (AlGaAs),[31] and titania (TiO_2).[20,32−35] To date, no reports have been shown in this field on silicon germanium (SiGe) alloys, despite their clear advantage of exhibiting larger refractive indices with respect to pure Si[36,37] allowing, in principle, for better light confinement. We note that, due to its high absorption in the visible region[36] that prohibits the formation of high quality resonances, germanium alone is not a desirable material for MR fabrication.[38,39] Nevertheless, the use of Ge with Si for dewetting provides a strategic tool for controlling the dynamics of island formation: it allows for tuning the island densities (e.g., higher[40] for the case of spontaneous dewetting, or lower[29] when using templating for guiding the dewetting fronts) speeds-up the self-assembly, allowing for a reduced processing temperature and overall dewetting time and controls the islands' shape by increasing the vertical aspect ratio. In contrast with more conventional fabrication approaches (e.g., e-beam lithography and reactive ion etching) where only cylinders can be obtained, our hybrid top-down/bottom-up method of "templated dewetting" of SiGe enables a true 3D shaping of the islands. Furthermore, it has recently been shown that the use of SiGe for dewetting can lead to complex arrangements (e.g., bimodal size distributions) of precisely positioned islands: a clear first step to more complex optical functions and more "striking" results with Mie resonator oligomers.[29] Furthermore, the use of SiGe coupled with Ge condensation has allowed for the implementation of core−shell structures integrated in the dewetted islands for the first time.[40] Very importantly, the integration of SiGe-based heterostructures within dewetted islands may lead to the implementation of light emitters in the resonators. This elusive point in the community of Mie resonators has been recently addressed for NIR frequencies emission with pure Ge antennas,[41,42] confirming the potential of this approach with respect to other dielectric nonemitting materials.

From an optical point of view, the imaginary component of the refractive index of pure Ge is orders of magnitude higher than for pure Si over a large part of the visible spectral region (see Supporting Information), explaining the need to minimize the concentration of Ge in SiGe alloys if nanostructures displaying low absorption at short visible wavelengths are to be obtained. This constraint is less important at near-infrared frequencies where Ge absorption is reduced. This observation opens the opportunity to use larger Ge concentrations exploiting a larger refractive index enhancing the light confinement and obtaining sharper resonances.[21]

Solid state dewetting has been extended to amorphous silicon on arbitrary silica substrates,[24] thus, relaxing the requirement to use commercial monocrystalline SOIs and allowing for a precise tuning of the buried oxide (BOX) thickness, which has been shown to strongly influence the resonant wavelengths of MRs.[3] Furthermore, using amorphous layers allows one to functionalize a full substrate at temperatures under 600 °C for Si-based resonators[43,44] and lower than 300 °C for Ge-based systems in only 30 min.[45] An intermediate temperature and comparable time scale are therefore expected for SiGe alloys.

This work centers on the use of arrays of resonant particles formed by templated dewetting of SiGe films in order to produce wavelength-tunable visible domain color filters working in reflection/transmission as well as in diffusion. The substrate-coupling phenomenon is refined with a semi-isolating oxide layer of an optimized thickness to create filters displaying narrow, tunable pass-bands. The association of thermal dewetting with a minimized templating step allows us to combine the advantages of both techniques: large surface treatment for the former and precise control of particle size and position for the latter. Care has been taken to address the integration of the filters with existing fabrication constraints on semiconductor imaging devices. To this end, the structures are all-dielectric (i.e., no metallic inclusions that could disrupt the charge transport in optoelectronic devices) and feature an optically and electrically isolating SiO_2 layer. We demonstrate the feasibility of our technique for the fabrication of practical filters by fabricating arrays with varying pass bands with dimensions of 15 × 15 μm^2, similar to the pixel size commonly used in CMOS/CCD imaging devices.

SIMULATIONS

The spectral position and efficiency of pass-band MR-based filters depend on a large number of coupled parameters, including the refractive index of the materials, resonator size and shape, array periodicity, isolation with respect to the substrate, and more. The simulations to determine the optimal parameters for our band-pass filters were performed on a homemade FDTD code written in C++. We chose to restrict the lateral (in-substrate-plane) arrangement of MRs to a square lattice. The refractive indices used in the simulations were $n_{Si/SiGe,sim} = 4$, $n_{SiO_2,sim} = 1.5$, $k_{Si/SiGe/SiO_2,sim} = 0$. More details on the simulation methods can be found in the Supporting Information.

Initial simulations were focused on determining the required aspect ratio for the MRs, defined as $\eta = h/r$, assuming an ellipsoid structure. Resonators with a low aspect ratio couple strongly the incident light with the substrate due to their high cross-section with the substrate with respect to their overall volume[2]; they give rise to wide, low contrast pass-bands unsuitable for our purpose. Increasing the aspect ratio of the resonators allows for better defined pass-bands, with acceptable performances for $\eta \sim 1$.[3] This is the main reason for using small amounts of Ge in the alloy: while pure Si dewetting leads to a

DOI: 10.1021/acsphotonics.6b00944
ACS Photonics 2017, 4, 873−883

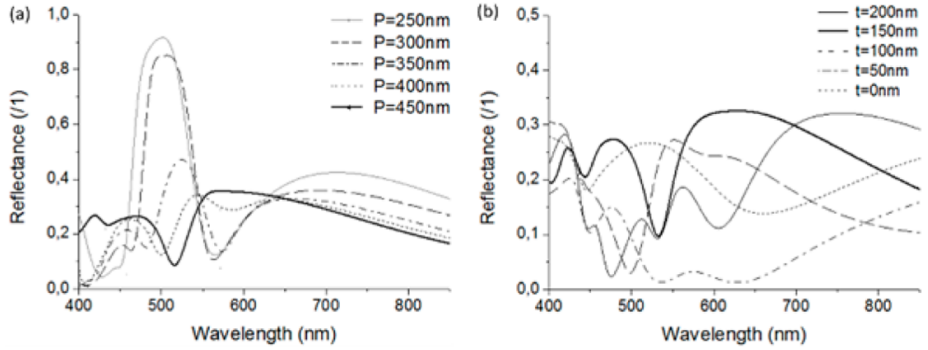

Figure 1. Simulated reflectance spectra for (a) various lateral periodicities P for hemispherical resonators of radius 90 nm on a Si substrate topped with 150 nm of SiO_2. (b) Various SiO_2 layer thicknesses t for hemispherical resonators of radius 90 nm in an array of periodicity 450 nm.

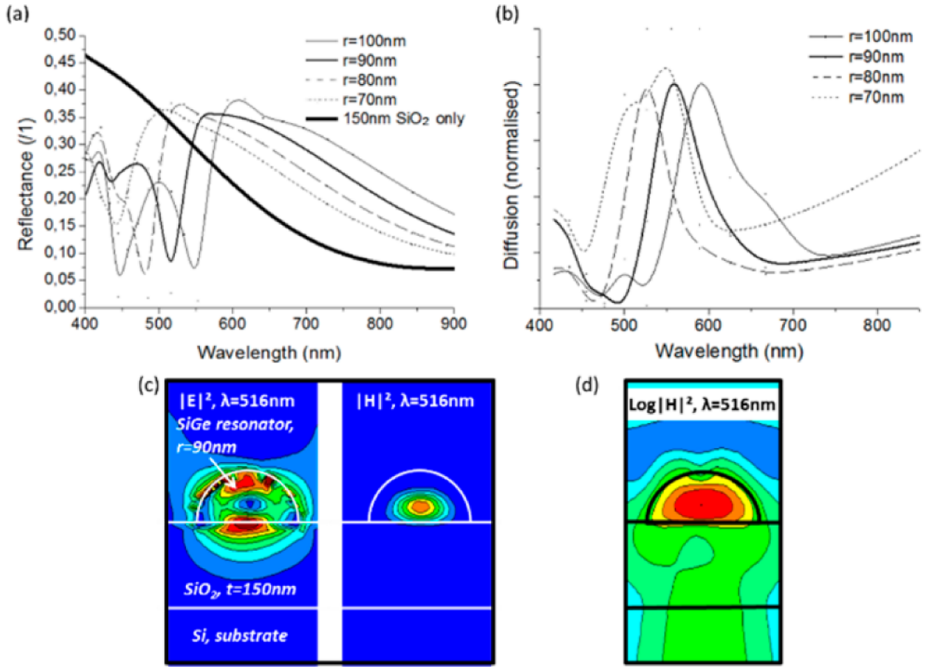

Figure 2. (a) Reflectance and (b) diffusion spectra for hemispherical resonators with various radii r in an array of 450 nm periodicity on a Si substrate topped with 150 nm of SiO_2. Also shown for comparison is the simulated spectral response of a Si substrate coated with the same SiO_2 thickness without resonators. (c) Electric and magnetic near-field profiles at the reflectance dip at λ = 516 nm for hemispheres of radius r = 90 nm. (d) Logarithm of magnetic near-field profile.

limited η (see, for instance, ref 27), a small Ge content transforms the shape into hemispheres (see refs 49 and 50), providing a more suitable shape ($\eta \sim 1$) for achieving sharper photonic resonances.

Next, we investigate the effect of the array periodicity on the filter performances. Figure 1a shows the simulated reflectance for an array of hemispherical MRs of radius 90 nm for various periodicities (P) atop 150 nm SiO_2. For low values of P (<350 nm), low full width half maximum (fwhm; <100 nm) peaks approaching 100% reflection efficiency can be seen in the reflectance spectra around 500 nm, superimposed on a low reflectance background. Although such characteristics are relevant to a special class of filter featuring an "inversed" pass-band (wherein light at all but a narrow wavelength range is efficiently coupled to the substrate), fabrication constraints have to-date prevented the realization of such structures via solid state dewetting. As the periodicity of the array increases, the reflectance peak reduces in amplitude, eventually giving way to a less pronounced dip for P > 400 nm. The degradation of the filtering properties on increasing P is to be expected, as the portion of the surface area covered by the resonators, linked to the light−matter interaction cross-section, is reduced.

A further parameter to be considered is the thickness t of the BOX layer separating the MRs from the substrate. It has already been shown in the literature[2,3] that, if the oxide thickness is of the order of the wavelength of incoming light, this layer can act as a Fabry−Perot cavity whereby it effectively determines the wavelengths available to undergo resonance in the MRs through constructive or destructive interference phenomena upon reflection. Furthermore, if this layer is too thick then light at resonant wavelengths is poorly coupled to the substrate, while if it is too thin resonances are broadened and their contrast decreased (see Figure 1b). From the analysis performed for an array of hemispheres of radius r = 90 nm with a periodicity P = 450 nm a single pronounced dip in reflectance is observed for t = 100 nm and slightly red-shifted,

DOI: 10.1021/acsphotonics.6b00944
ACS Photonics 2017, 4, 873−883

at t = 150 nm. These two values therefore constitute the bounds of the acceptable range of t.

Clearly, the most critical parameter to be set is the resonator's optical volume, by which we mean the product of the physical volume and the material refractive index, as this determines the wavelengths of the Mie resonances. Naturally, a greater volume yields resonances that are red-shifted with respect to those of smaller resonators, together with permitting higher order modes (e.g., electric and magnetic quadrupoles[2]). For a hemispherical resonator, the volume can be simply translated to the radius of the particle. Figure 2a shows the simulated reflectance and Figure 2b shows the simulated diffusion spectra of hemispherical resonators with varying radii in arrays of periodicity P = 450 nm on a Si substrate with an oxide thickness t = 150 nm. A common reflectance dip occurs at 450 nm, equal to the array periodicity, corresponding to the Rayleigh anomaly where the first diffracted order in the air above the system ceases to exist. This dip is more pronounced for resonators with larger radii, as the diffraction efficiency of the 2D grating that the array constitutes is increased. The center wavelength of the reflectance dip corresponding to the Mie resonance mediated pass-band is clearly seen to red-shift upon increasing the particle radius, passing from λ = 450 nm for r = 70 nm (where the reflectance dip is superimposed on the Rayleigh anomaly) to λ = 550 nm for r = 100 nm. We see a similar red-shift of the diffusion peaks in Figure 2b.

Further to the fact that the pass-bands are seen to occur near the resonant wavelengths, the FDTD simulations allow us to gain an insight into the phenomena giving rise to their formation. Figure 2c shows the near field distributions of the electric and magnetic fields at the wavelength corresponding to the reflectance minimum for r = 90 nm in Figure 2a: a magnetic field node is centered in the hemispherical resonator encircled by an electric displacement current. This confirms that the fundamental Mie resonances are indeed responsible for the features observed in the simulated spectra. Upon plotting the logarithm of the magnetic field distribution (Figure 2d), it is clearly seen that the field associated with the resonance also extends through the BOX layer into the Si substrate, constituting the substrate-coupling phenomenon which provides the selective transmittance needed to tune the filter pass-bands. In order to demonstrate the efficiency of the combined BOX-resonator array structure on modulating the reflectance spectra, Figure 2a also shows the simulated response of a Si substrate coated only with 150 nm SiO_2. It can be seen that no rapid modulation of the reflectance, needed to create spectrally narrow filters, is observed without the additional presence of the Mie resonator arrays.

To summarize, we can conclude from the simulations that the optimal geometry for the SiGe-based MRs filters is hemispherical islands with radii varying between roughly 70 and 150 nm atop 100−150 nm of SiO_2 on a silicon substrate.

EXPERIMENTAL SECTION

The outcome of the simulations calls for a very unique silicon−germanium on insulator (SGOI) structure, particularly in terms of the SiO_2 BOX thickness, which is not commercially available. We have therefore resorted to fabricating our own custom SGOI structures. As mentioned earlier, in order to obtain MRs with an aspect ratio close to 1, we have added Ge to the Si thin film on top of the BOX. We limit the percentage of Ge to around 20% ($Si_{0.8}Ge_{0.2}$) in order to yield hemispherical islands while avoiding strong optical absorption in the visible spectral region.[46−48] Such concentrations are, however, large enough to induce dramatic modifications of the dewetting dynamics and of the equilibrium shape of SiGe islands:[49,50] a vertical aspect ratio of ∼1 and improved in-plane symmetry can be obtained via Ge alloying during dewetting in contrast with pure Si featuring very flat islands.

Two samples were fabricated, named A and B, with thicknesses of 30 and 50 nm for the initial flat SiGe layer, respectively. As detailed in the Methods section, these thicknesses allow us to achieve MRs of the dimensions required with a relatively low periodicity that is typically below the pass-band wavelength. For both samples the BOX thickness was 150 nm. The key steps of the fabrication process are shown in Figure 3a.

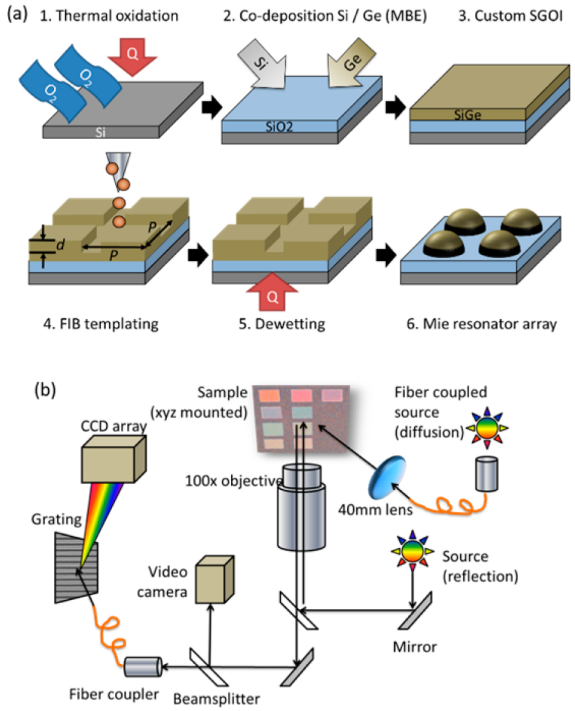

Figure 3. (a) Diagram showing the steps involved in the fabrication of MR arrays. Panel 4 shows the periodicity P and milling depth d. (b) Spectroscopy bench used for reflectance and diffusion measurements.

The custom SGOI substrates were prepared via a two-step process; first, thermal oxidation of crystalline Si wafers was carried out in a rapid thermal processing oven, followed by deposition of the SiGe alloys under ultrahigh vacuum (UHV) in a molecular beam epitaxy (MBE) reactor. The samples were then transferred to a mass-filtered liquid-metal ion source FIB (LMIS-FIB) milling system for templating prior to dewetting. Groups of square lattices approximately 15 × 15 μm^2 in size were milled, featuring periodicities of 250, 290, 330, 360, 400, 450, 500, 550, and 600 nm in both spatial directions in order to yield resonators with the sizes determined previously by the simulations (radii ranging from 70 to 150 nm). Eight groups of lattices (each with 250 ≤ P ≤ 600 nm) were milled on each sample, with four different nominal target milling depths, d: 2, 4, 6, and 7 nm. After ion milling, the samples were then returned to the UHV chamber of the MBE reactor for dewetting (annealing) at 700 °C for 30 min. After annealing, the dewetted islands are no longer constituted of amorphous

DOI: 10.1021/acsphotonics.6b00944
ACS Photonics 2017, 4, 873−883

material, but are made up of polycrystalline SiGe.[28] This transition to a polycrystalline phase has been demonstrated in the literature to lead to narrower and intensified resonances.[21]

The samples were initially characterized by bright- and dark-field optical microscopy in order to observe the reflected and diffused colors, as well as to obtain an indication of the homogeneity of the resonator arrays formed. Following this, diffusion and reflection spectra at visible and near-infrared frequencies were collected on a homemade spectroscopy bench, shown in Figure 3b. The samples were further characterized by atomic force microscopy (AFM) and scanning electron microscopy (SEM).

OPTICAL CHARACTERIZATION RESULTS

The palettes in Figure 4 show the reflected and diffused colors observed with the imaging optical microscope as a function of the array periodicity P and the milling depth d for samples A and B. Patterns sharing the same milling depth are arranged on a same row, with the period increasing from left to right. The effect of these two parameters on the size of the MRs formed after dewetting is best understood through the diffused colors: for a given d, increasing P yields larger resonators as shown by the diffused color transitioning from short to long wavelengths (e.g., blue to red for sample A on row d = 6 nm, from r1 to r5), as expected. For the highest periodicities, the diffused colors begin to taint blue due to the MRs supporting multiple resonant modes, as discussed in more detail in the spectroscopic measurement analysis. At a fixed periodicity, increasing the milling depth yields smaller resonators due to the fact that deeper milling sputters more material and the diffused colors blue-shift.

For the remaining characterizations, we have focused for sample A on the line of pixels formed at milling depth d = 6 nm, and for sample B on the line corresponding to d = 2 nm, since these yield diffused colors covering the entire visible spectral region. These pixels are numbered r1−r9 in Figure 4. Referring to Figures 5a,c and 6a,d, showing the collected diffusion (D) and reflectance (R) spectra for these pixels, the general trends can be summarized as follows: as the resonator size increases, the peaks in the diffusion spectra are seen to shift from blue to red (r2 through to r7/8), as well as multiplying in number for the highest periodicities (r6, r7, and r8), corresponding to the presence of multiple resonance orders in the islands. In the reflectance spectra, minima can be observed at spectral positions near the diffusion peaks due to the substrate coupling phenomenon described in the Simulations section. Either side of these minima, the reflectance spectra are seen to exhibit maxima whose positions determine the apparent reflected color of the arrays. The trends described previously in the experimental reflectance spectra presented in Figure 6a,d are in good qualitative agreement with the simulation results. Further simulations presented in the Supporting Information (taking into account the true sizes of the resonators as measured and presented in the Physical Characterization Results section) allow for a direct comparison between the simulation and experimental results. We note that in order to estimate the transmittance T of the MR arrays, representing the intensity received by a photosensitive structure buried in the substrate and featuring the pass-bands mentioned previously, the simple expression $T = 1 - R$ can be used (assuming the absorption in the resonators to be negligible). The investigation of R for both samples in spontaneously dewetted areas (such as those shown on the right of each

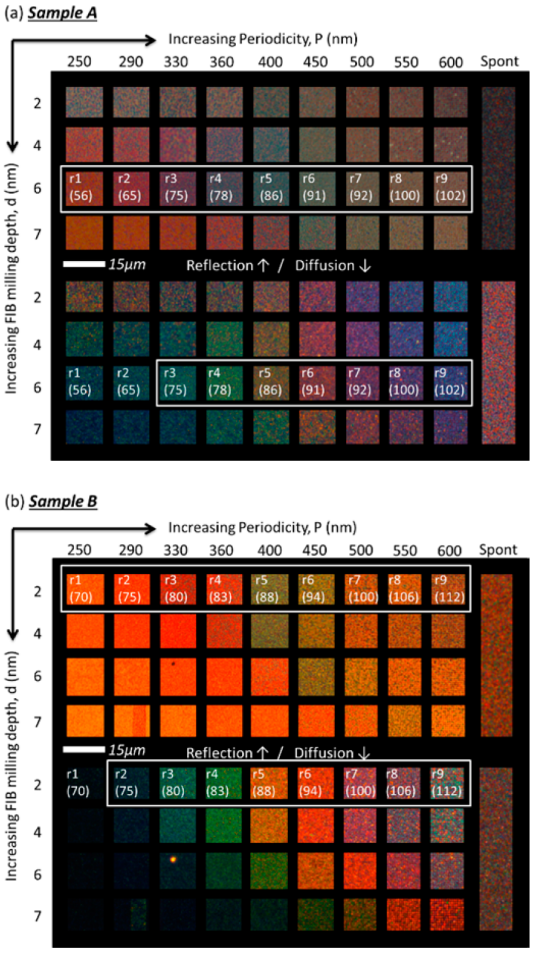

Figure 4. Palettes formed from bright-field (reflectance) and dark-field (diffusion) optical images of resonator arrays of varying periodicities P with different templating milling depths d (a) on sample A, (b) on sample B. To the right of each panel (columns labeled "Spont") is an image of the spontaneously dewetted region of each sample viewed in both bright- and dark-field. The numbering of arrays is used in the optical and physical characterizations, while arrays in white boxes are those whose CIE chromaticity coefficients feature in Figures 5 and 6. The numbers in brackets correspond to the estimated resonator radii in nm, as reported in Figure 7c for sample A. Each 15 × 15 μm^2 dewetted pattern is here surrounded by a black cornice in order to better highlight and compare the reflected and scattered colors. An image of the original configuration of the sample is provided in Figure S3 in the Supporting Information only for the specific cases of 6 nm milling depth of sample A (third line of the palette in (a)) and 2 nm milling depth for sample B (first line of the palette in (b)). In Figure S3 (Supporting Information), the spontaneously dewetted areas between the etched patterns are not masked with a black cornice. For the sake of thoroughness, SEM images including patterned and unpatterned areas are displayed in Figure 7 (a).

palette in Figure 4) is shown in the Supporting Information. Even though this discussion goes beyond the aim of this paper, we note that spontaneous dewetting could be exploited for the fabrication of broad-band and broad-angle antireflection coatings. In fact, disordered systems may outperform their ordered counterparts as has been shown recently.[51,52] A hint of this possibility can be found in the lower reflected intensity of the spontaneously dewetted region in Figure 4a and quantified by the low reflectivity spectrum shown in the Supporting

DOI: 10.1021/acsphotonics.6b00944
ACS Photonics 2017, 4, 873−883

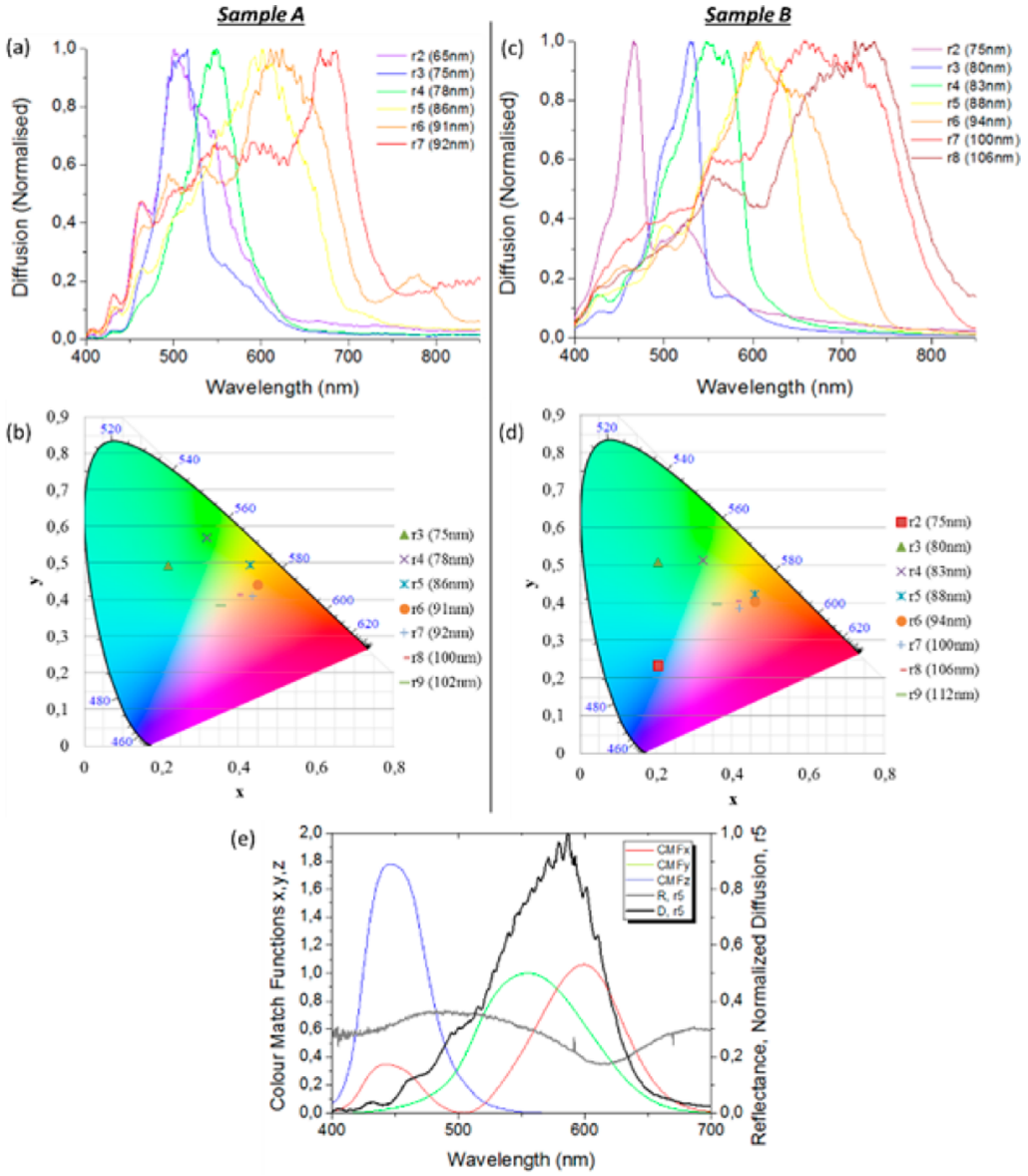

Figure 5. (a, c) Scattering spectra for selected pixels on samples A and B, respectively, each curve is self-normalized. (b, d) CIE chromaticity gamut for selected pixels on samples A and B, respectively, based on the scattering spectra. The numbers in brackets correspond to the estimated resonator radii in nm. (e) Color matching functions used to calculate chromaticity coordinates and reflectance and diffusion spectra for array r5 on sample A.

Information in Figure S3d ($R \sim 10\%$ over a broad spectral range). Nonetheless, this task would require a large reduction of the BOX thickness underneath the SiGe resonators, as shown by the simulations in Figure 1b. From a fundamental research point of view, it is worth mentioning that disordered arrays of resonators could be extremely appealing for the investigation of light diffusion in complex media.[53−56]

To complete the optical characterization of the samples, and to quantify the filters' performances in a standardized way, the chromaticity coefficients have been calculated and placed on the color space (gamut) defined by the 1931 Commission Internationale de l'Eclairage (CIE) for the pixels indicated by white boxes on the color palettes in Figure 4. First, the X, Y, Z chromaticity components are calculated using eq 1, and the analogous versions for the Y and Z components, by integrating the spectral response of the pixels in both reflectance $R(\lambda)$ and diffusion $D(\lambda)$ configurations with the corresponding color matching functions (CMF) $\overline{x}$, $\overline{y}$, $\overline{z}$ shown in Figure 5e. We note here that a "flat" (nonwavelength-dependent) source has been used in the calculations, such that the colors plotted represent the unconvoluted performances of the filters. The reduced parameters x, y are then calculated using eqs 2 and 3.

$$X = \int R,\ D(\lambda)\overline{x}(\lambda)\mathrm{d}\lambda \tag{1}$$

$$x = \frac{X}{X + Y + Z} \tag{2}$$

$$y = \frac{Y}{X + Y + Z} \tag{3}$$

Figures 5b,d and 6b,e show the coordinates of selected pixels on both samples operating in diffusion and reflection

DOI: 10.1021/acsphotonics.6b00944
ACS Photonics 2017, 4, 873−883

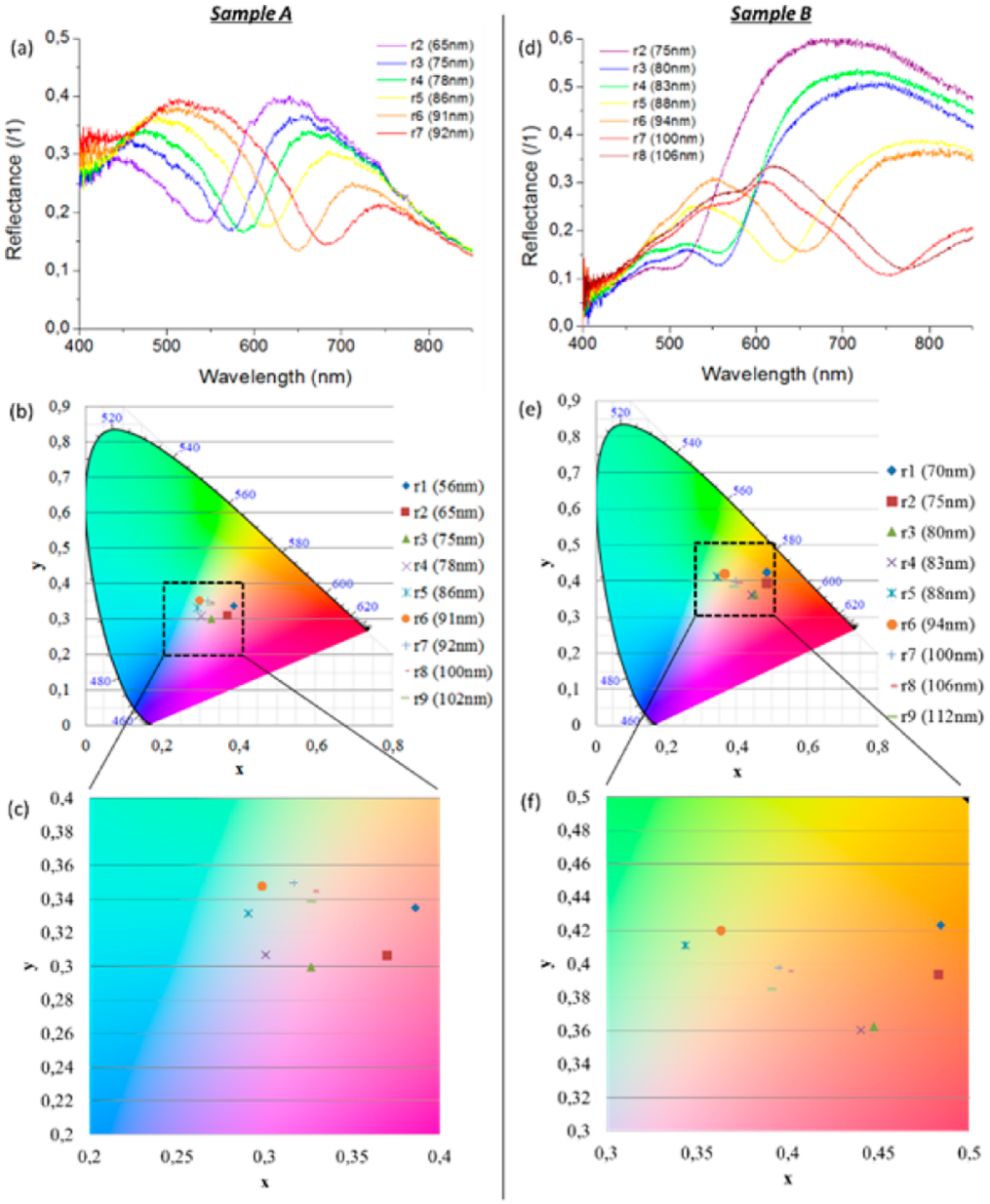

Figure 6. (a, d) Reflectance spectra for selected pixels on samples A and B, respectively, (b, e) CIE chromaticity gamut for selected pixels on samples A and B, respectively, functioning in reflection, (c) zoom on central region of (b), (f) zoom on central region of (e). The numbers in brackets correspond to the estimated resonator radii in nm.

respectively on the full color space, while Figure 6c,e are zooms on the indicated central regions. In both reflection and diffusion configurations, and for both samples A and B, the plotted coordinates encircle the white-point indicating that a full color palette is available with the filters. The radial distance from the white-point is lower in the reflection configuration, owing to the high "background" seen in the reflectance spectra from which the pass-band peak is subtracted making the filters less efficient. The purity of the filtered colors is highest for the smallest MRs (i.e., r1 is less "white" than r9), due to the fact that the larger islands support multiple resonant modes.[2] This accounts for the "spiralling-in" toward the white-point of the plotted coordinates with increasing MR size. Comparing samples A and B, it can be seen that the "quality" of the colors obtained with sample B is higher due to the increased radial distance from the white-point that is typically observed.

It is worth stressing that, in spite of a larger extinction coefficient of Ge with respect to Si at shorter wavelengths (see Supporting Information, Figure S2b) where the dielectric Mie resonators exhibit only the lowest order resonances (the broadest), a relatively high Q factor can be found: as an example, the case of r2 in Figure 5c shows a resonance at 460 nm with a Q factor of about 13. This value of Q for 20% SiGe compares well with the values reported for pure Si at the same frequencies.[2,57] At the same time this measured value of Q clearly outperforms the case of pure Si dewetting (shown ref 27 where the islands featured a low η) accounting for the beneficial effect of an appropriate shape of the resonant particles ($\eta \sim 1$).

DOI: 10.1021/acsphotonics.6b00944
ACS Photonics 2017, 4, 873−883

PHYSICAL CHARACTERIZATION RESULTS

The SEM images of arrays r1−r9 on sample A, shown in Figure 7a, reveal that the organization of the islands on a square lattice

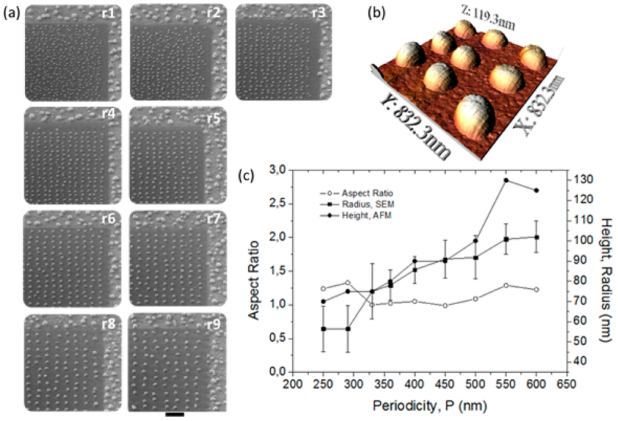

Figure 7. (a) SEM images of the corners of arrays r1−r9 of sample A. Black scale bar = 1 μm. (b) AFM image of islands in array r2 on sample B. (c) Aspect ratio, in-substrate-plane radius, and orthogonal height as a function of lattice periodicity for arrays r1−r9 on sample A.

is maintained for periods at or over 330 nm (i.e., r3 and above). As expected, the resonators are seen to increase in size as the array periodicity rises, and the size dispersion within a given array is relatively low leading to the overall homogeneity of the colors observed in the diffusion and reflection measurements. The AFM measurements also enable us to estimate the true aspect ratio of the MRs, which is found to vary between 1 and 1.3 suggesting that the islands are indeed hemispherical to a first approximation. This is further illustrated in Figure 7b, showing an AFM image of nine islands in array r2 on sample B. The in-substrate-plane radius of the MRs determined from the SEM images and their heights from the AFM scans are plotted together with the calculated aspect ratio as a function of the array periodicity in Figure 7c, where each data point represents a pixel (from r1 to r9).

The structural characterization accounts for the qualitative differences found between the FDTD simulations shown in Figure 2a and the experimental outcome. As can be seen from the error bars in Figure 7c, a dispersion of the islands' dimensions of between ±10% and ±20% from the average value is observed. The effect of this dispersion is to "blur" the minima of reflected intensity and so broaden the fwhm of the pass-bands from near 50 nm in the simulations to approximately 100 nm in the measured data, while at the same time reducing the depth of the measured pass-band minima.

In spite of the measured size dispersion, the diffusion spectra have similar broadening (fwhm) to those obtained with other techniques. In this case the resonant part of the light can be isolated and the relatively large gap between the islands is not an issue. Another important origin of disorder is the use of amorphous layers leading to less controlled dewetting due to a random formation of grains in the polycrystalline islands and resulting in inhomogeneous distributions of shapes. For the sake of thoroughness we note that for smaller etching periodicities the spatial organization of the dewetted islands is less precise with respect to larger periodicities (e.g., compare r1 with r9 in the SEM images shown in Figure 7a). This fact is mainly ascribed to spurious effects induced by the limited lateral resolution of FIB etching having a larger impact for smaller periodicities. Nonetheless, in spite of a poorer spatial organization of the islands, arrays featuring smaller periodicity exhibit the best performances in terms of spectral selectivity in both diffusion and reflection configurations, thus, accounting for the relevance of this approach at shorter wavelengths. Better results could be obtained by using lower milling currents (at the price of a longer milling time) or exploiting better performing etching methods, such as e-beam lithography. Finally, we note that the use of monocrystalline SOI associated with in situ Ge deposition successfully allows one to limit size, shape, and position fluctuations of the islands to within the range of a few percent.[29]

As mentioned earlier, the quality of color filtering in reflection is lower with respect to diffusion due to the high background on which the resonances are superposed. Apart from size and shape-related issues, the main reason for this background is the relatively large spacing of the islands leading to a poor interaction between the impinging light and the MRs. Indeed, in the experimental results we note that the best results in filtering are obtained at smaller periodicities. The easiest way to prevent this problem is to swell the islands further after their formation by supplying additional SiGe after the annealing step in the MBE. Moreover, the use of even thicker initial layers of SiGe should enable the implementation of the same kind of filters at near-infrared frequencies, also benefiting from reduced absorption losses of SiGe with respect to visible frequencies (not shown).

CONCLUSION

We have demonstrated that SiGe alloys are a valuable alternative to pure Si in manipulating light at the nanoscale with Mie resonators. Reflection and diffusion filters can be formed via dewetting of amorphous layers previously milled with square lattices of varying pitch. The ability to tune the operating wavelength by varying the size of the islands allows for a flexible design that can be adapted to any number of applications. The fabrication technique used allows for the rapid elaboration of large surface area filters and is compatible with existing semiconductor processing techniques due to the relatively low temperature involved. We note that the use of SiGe-based alloys in novel electronic devices, such as FET and C-MOS transistors, is nowadays extremely important. Because of this, opening the field of dielectric MRs to SiGe-based semiconductor alloys is an important step forward toward the integration of photonics with electronic devices.

METHODS

Sample Preparation. The custom SGOI substrates were prepared by thermal oxidation of crystalline Si (100) wafers in a rapid thermal processing oven (Jipelec JetFirst). The required oxide thickness of 150 nm was obtained through a cumulative total of 50 min at 1000 °C, split into 5 equal steps to avoid excessive thermal stress on the oven. The oven chamber was first pumped down to approximately 1 Torr before being flushed continuously during the growth process with Oxygen at a rate of 200 sccm. The oxidized wafers were then inserted into the chamber of a molecular beam epitaxy reactor (MBE, Riber), in which the pressure was maintained between 10^{-9} and 10^{-10} Torr (ultrahigh vacuum, UHV) during the deposition of the SiGe alloy. In the case of sample A, Si and Ge were codeposited

DOI: 10.1021/acsphotonics.6b00944
ACS Photonics 2017, 4, 873−883

at a rate of 16.5 and 4.1 Å/min, respectively, for 14.5 min, yielding a 30 nm film. For sample B, the rates were 14.1 (Si) and 3.5 Å/min (Ge), and the deposition duration 28.4 min, yielding a 50 nm film. The ratio of the deposition rates (4:1) corresponds to an alloy composition of $Si_{0.8}Ge_{0.2}$. The wafers were not heated during the deposition, yielding amorphous films.

The samples were then transferred to an LMIS-FIB milling system (COBRA-type dual beam workstation from Orsay Physics operating at 30 keV) for templating prior to dewetting. Groups of square lattices approximately 15 × 15 μm^2 in size were milled. The milling was performed at a current of ∼30 pA using Si^{2+} ions selected from an AuSi source and the total milling time was approximately 30 min, corresponding to an average of 30 s per 15 × 15 μm^2 lattice.

The following periodicities between the straight line segments making up the lattices were chosen: 250, 290, 330, 360, 400, 450, 500, 550, and 600 nm. This range of periods was used on both samples (A and B) and was chosen in order to yield islands with dimensions comparable to those previously determined in the simulation section by the following reasoning: It is known that for sufficiently small patches (i.e., squares having sides smaller or similar to the characteristic length scale of the underlying dewetting instability), all the mass present in a patch collapses into an individual island (see, for instance, ref 29). The area of SiGe film required to form a hemispherical resonator of radius r from a film of thickness t is $A = (2\pi r^3)/(3t)$. The periodicity P_i in this ideal case, where the trench cut by the LMIS-FIB beam is infinitely narrow is therefore $P_i = \sqrt{A}$. However, the effective width (i.e., that providing an equivalent volume of sputtered matter for a trench extending through the entire SiGe layer) of the lines milled by the LMIS-FIB was estimated to be ∼100 nm, so the true period required for the lattice is $P = P_i + 100$. The simulations showed that resonators with radii between 70 and 150 nm are required, which correspond to lattice periods between 255 and 585 nm for a SiGe film depth of 30 nm (here referring to sample A). It is arguable that any initial SiGe film thickness could be used, providing the periodicity of the FIB patterning is correctly chosen to yield hemispherical islands of the size wanted. However, in order to avoid spectral features associated with the cutoff of the first diffracted order (Rayleigh phenomenon) that are detrimental to the filters' performances, the lateral period of the islands must be lower than wavelength of operation of each filter array, thus, providing a lower limit to the initial film thickness. The thicknesses of the initial SiGe films (30 nm for sample A and 50 nm for sample B) were chosen to take this constraint into account. Eight groups of lattices (each with 250 $\leq P \leq$ 600 nm) were milled on each sample, with four different target thicknesses (each repeated twice): 2, 4, 6, and 7 nm. Interestingly, we therefore note that even if the SGOI layer is not completely milled down to the BOX, after annealing a uniform array of isolated MRs can be obtained. This observation is in contrast with the case of monocrystalline SOI, where a noncomplete etching leads to a flattening of the milled trenches during annealing, thus losing the islands' organization. This difference may be explained by the complex island formation dynamics in amorphous layers associated with recrystallization during annealing and grain formation.[43]

After ion milling the samples were then returned to the UHV chamber of the MBE reactor for dewetting (annealing). During the transfer process, the samples were immersed in a 4% concentration aqueous HF solution for 5 s in a nitrogen atmosphere to eliminate any native oxide layer formed on top of the SGOI. The temperature ramping used for the dewetting in ultrahigh vacuum was composed of an initial plateau at 500 °C for 30 min to further clean the SGOIs by removing any dirt or organic residues from the surface, followed by a main plateau at 700 °C for 30 min during which the dewetting occurs. Similar results can be obtained at lower temperatures and longer annealing times.

Optical Characterization. The samples were characterized by bright- and dark-field microscopy (with a LEICA DMI5000 M microscope at 100× magnification, NA = 0.75) in order to observe the reflected and diffused colors, as well as to obtain an indication of the homogeneity of the resonator arrays formed. In the dark-field configuration, the cone of light supplied by the halogen source used to probe the sample is centered at 70° from the sample surface normal, with collection occurring at all angles allowed by the NA of the objective lens. Following this, diffusion and reflection spectra were collected on a homemade spectroscopy bench, shown in Figure 3b. For reflection measurements, diffused light from a high-power halogen source was focused into the back-focal-plane of a 100× Mitutoyo Plan Apo NIR objective (NA = 0.7), giving a near-collimated plane-wave illumination source on the sample surface. For diffusion measurements, light from a secondary fiber-coupled halogen source was focused onto the sample surface with a lens of focal length 35 mm at ∼70 degrees from the surface normal. The reflected/diffused light was then collected by the same objective lens used for illumination in the reflectance configuration. The signal was focused onto a multimode optical fiber acting as confocal pinhole and allowing us to select the light reflected/diffused from a circular area with a diameter of approximately 5 μm in the sample plane. Thus, the spectral investigation is performed over several islands integrating the optical properties over many repetitions of nominally identical MRs. Finally, through the fiber, the light is fed into a spectrometer (Acton IsoPlane SCT-320) equipped with a 150 gpmm, 500 nm blazed grating, and finally imaged onto a Si-CCD array (Princeton Pixis 100).

Physical Characterization. Sample A was characterized by atomic force microscopy (AFM) during which 2.5 × 2.5 μm^2 regions of selected resonator arrays were imaged in order to extract the heights of the islands from line profiles following the scan direction. The same arrays were characterized by scanning electron microscopy (SEM) in order to estimate the in-substrate-plane diameter of the islands and examine the array regularity. The sample was oriented at an angle of 45° relative to the incidence of the electrons, and the lateral field of view was 5.75 μm. For each array, the top right-hand corner was imaged so as to show the contrast between the organization obtained through templated- and spontaneous-dewetting, as shown in Figure 7. The average substrate-plane radius was estimated through the measurement of 10 islands in the lower left corner of each image via pixel counting.

■ ASSOCIATED CONTENT

Supporting Information

The Supporting Information is available free of charge on the ACS Publications website at DOI: 10.1021/acsphotonics.6b00944.

Details of the FDTD simulations, refractive indices of the SiGe alloy, and measurements on the spontaneously dewetted regions (PDF).

DOI: 10.1021/acsphotonics.6b00944
ACS Photonics 2017, 4, 873−883

AUTHOR INFORMATION

Corresponding Authors

*E-mail: tomwood321@hotmail.com.
*E-mail: marco.abbarchi@im2np.fr.

ORCID

Thomas Wood: 0000-0002-5279-2797

Present Addresses

‡INL, Ecole Centrale de Lyon, 36 Avenue Guy de Collongue, 69134 Écully, France.
‖GREMAN, UMR CNRS 7347, Université François Rabelais de Tours, 16 rue Pierre et Marie Curie, 37071 TOURS Cedex 2, France.

Author Contributions

The manuscript was written through contributions of all authors. All authors have given approval to the final version of the manuscript.

Funding

We acknowledge the Projects PHC MAGHREB (No. 32595SL), EMMAG-Erasmus Mundus Maghreb and Egypt, the A*MIDEX Project (No. ANR-11-IDEX-0001-02) funded by the Investissements d'Avenir; a French Government program managed by the French National Research Agency (ANR), the SATT-Sud Est Project PROMETHEUS, the Nanotecmat Platform of the IM2NP Institute of Marseille and the CP2M microscopy center of Aix-Marseille University. The authors thank Rachel V. Zucker and Dominique Chatain for the useful discussions.

Notes

The authors declare no competing financial interest.

REFERENCES

(1) Mie, G. Beitrage zur Optik truber Medien speziell kolloidaler Goldlo sungen (Contributions to the optics of diffuse media, especially colloid metal solutions). *Ann. Phys.* **1908**, *330*, 377−445.
(2) Coenen, T.; Van De Groep, J.; Polman, A. Resonant modes of single silicon nanocavities excited by electron irradiation. *ACS Nano* **2013**, *7* (2), 1689−1698.
(3) Van de Groep, J.; Polman, A. Designing dielectric resonators on substrates: Combining magnetic and electric resonances. *Opt. Express* **2013**, *21* (22), 26285.
(4) Krasnok, A.; Makarov, S.; Petrov, M.; Savelev, R.; Belov, P.; Kivshar, Y. Towards all-dielectric metamaterials and nanophotonics. *Proc. SPIE* **2015**, 950203.
(5) Spinelli, P.; Verschuuren, M. A.; Polman, A. Broadband omnidirectional antireflection coating based on subwavelength surface Mie resonators. *Nat. Commun.* **2012**, *3*, 692.
(6) Brongersma, M. L.; Cui, Y.; Fan, S. Light management for photovoltaics using high-index nanostructures. *Nat. Mater.* **2014**, *13*, 451.
(7) Jahani, S.; Jacob, Z. All-dielectric metamaterials. *Nat. Nanotechnol.* **2016**, *11*, 23.
(8) Decker, M.; Staude, I. Resonant dielectric nanostructures: a low-loss platform for functional nanophotonics. *J. Opt.* **2016**, *18* (10), 1−31.
(9) Spinelli, P.; Macco, B.; Verschuuren, M. A.; Kessels, W. M. M.; Polman, A. Al2O3/TiO2 nano-pattern antireflection coating with ultralow surface recombination. *Appl. Phys. Lett.* **2013**, *102*, 233902.
(10) Fu, D.; Song, J.; Yu, H.; Zhang, Z.; Wang, W.; Xu, Y.; Song, G.; Wei, X. Coupled optical and electrical study of thin-film InGaAs photodetector integrated with surface InP Mie resonators. *J. Appl. Phys.* **2016**, *119*, 103103.
(11) Yue, W.; Gao, S.; Lee, S.-S.; Kim, E.-S.; Choi, D.-Y. Subtractive Color Filters Based on a Silicon-Aluminum Hybrid-Nanodisk Metasurface Enabling Enhanced Color Purity. *Sci. Rep.* **2016**, *6*, 29756.
(12) Proust, J.; Bedu, F.; Gallas, B.; Ozerov, I.; Bonod, N. All-Dielectric Colored Metasurfaces with Silicon Mie Resonators. *ACS Nano* **2016**, *10* (8), 7761−7767.
(13) Zywietz, U.; Schmidt, M. K.; Evlyukhin, A. B.; Reinhardt, C.; Aizpurua, J.; Chichkov, B. N. Electromagnetic Resonances of Silicon Nanoparticle Dimers in the Visible. *ACS Photonics* **2015**, *2*, 913−920.
(14) Van De Groep, J.; Coenen, T.; Mann, S. A.; Polman, A. Direct imaging of hybridized eigenmodes in coupled silicon nanoparticles. *Optica* **2016**, *3* (1), 93−99.
(15) Staude, I.; Miroshnichenko, A. E.; Decker, M.; Fofang, N. T.; Liu, S.; Gonzales, E.; Dominguez, J.; Luk, T. S.; Neshev, D. N.; Brener, I.; Kivshar, Y. Tailoring Directional Scattering through Magnetic and Electric Resonances in Subwavelength Silicon Nanodisks. *ACS Nano* **2013**, *7* (9), 7824−7832.
(16) Evlyukhin, A. B.; Eriksen, R. L.; Cheng, W.; Beermann, J.; Reinhardt, C.; Petrov, A.; Prorok, S.; Eich, M.; Chichkov, B. N.; Bozhevolnyi, S. I. Optical spectroscopy of single Si nanocylinders with magnetic and electric resonances. *Sci. Rep.* **2014**, *4*, 4126.
(17) Coenen, T.; Van de Groep, J.; Polman, A. Resonant Modes of Single Silicon Nanocavities Excited by Electron Irradiation. *ACS Nano* **2013**, *7* (2), 1689−1698.
(18) Proust, J.; Bedu, F.; Chenot, S.; Soumahoro, I.; Ozerov, I.; Gallas, B.; Abdeddaim, R.; Bonod, N. Chemical Alkaline Etching of Silicon Mie Particles. *Adv. Opt. Mater.* **2015**, *3* (9), 1280.
(19) Wang, Z. Y.; Zhang, R. J.; Wang, S. Y.; Lu, M.; Chen, X.; Zheng, Y. X.; Chen, L. Y.; Ye, Z.; Wang, C. Z.; Ho, K. M. Broadband optical absorption by tunable Mie resonances in silicon nanocone arrays. *Sci. Rep.* **2015**, *5*, 7810.
(20) Bottein, T.; Wood, T.; David, T.; Claude, J. B.; Favre, L.; Berbézier, I.; Ronda, A.; Abbarchi, M.; Grosso, D. Black" Titania Coatings Composed of Sol−Gel Imprinted Mie Resonators Arrays. *Adv. Funct. Mater.* **2017**, *27* (2), 1604924.
(21) Zywietz, U.; Evlyukhin, A. B.; Reinhardt, C.; Chichkov, B. N. Laser printing of silicon nanoparticles with resonant optical electric and magnetic responses. *Nat. Commun.* **2014**, *5*, 3402.
(22) Dmitriev, P. A.; Makarov, S. V.; Milichko, V. A.; Mukhin, I. S.; Gudovskikh, A. S.; Sitnikova, A. A.; Samusev, A. K.; Krasnok, A. E.; Belov, P. A. Laser fabrication of crystalline silicon nanoresonators from an amorphous film for low-loss all-dielectric nanophotonics. *Nanoscale* **2016**, *8* (9), 5043−8.
(23) Kim, G. H.; Zucker, R. V.; Ye, J.; Carter, W. C.; Thompson, C. V. Quantitative analysis of anisotropic edge retraction by solid-state dewetting of thin single crystal films. *J. Appl. Phys.* **2013**, *113*, 043512.
(24) Zucker, R. V.; Kim, G. H.; Carter, W. C.; Thompson, C. V. A model for solid-state dewetting of a fully-faceted thin film. *C. R. Phys.* **2013**, *14*, 564.
(25) Zucker, R. V. Capillary-driven shape evolution in solid-state micro- and nano-scale systems. *Ph.D. Thesis*, Massachusetts Institute of Technology, 2015.
(26) Zucker, R. V.; Carter, W. C.; Thompson, C. V. Power-law scaling regimes for solid-state dewetting of thin films. *Scr. Mater.* **2016**, *116*, 143−146.
(27) Abbarchi, M.; Naffouti, M.; Vial, B.; Benkouider, A.; Lermusiaux, L.; Favre, L.; Ronda, A.; Bidault, S.; Berbezier, I.; Bonod, N. Wafer Scale Formation of Monocrystalline Silicon-Based Mie Resonators via Silicon-on-Insulator Dewetting. *ACS Nano* **2014**, *8* (11), 11181−11190.
(28) Naffouti, M.; David, T.; Benkouider, A.; Favre, L.; Ronda, A.; Berbezier, I.; Bidault, S.; Bonod, N.; Abbarchi, M. Fabrication of poly-crystalline Si-based Mie resonators via amorphous Si on SiO2 dewetting. *Nanoscale* **2016**, *8*, 2844−2849.
(29) Naffouti, M.; David, T.; Benkouider, A.; Favre, L.; Delobbe, A.; Ronda, A.; Berbezier, I.; Abbarchi, M. Templated Solid-State Dewetting of Thin Silicon Films. *Small* **2016**, *12*, 6114.
(30) Albella, P.; De La Osa, R. A.; Moreno, F.; Maier, S. A. Electric and magnetic field enhancement with ultralow heat radiation dielectric nanoantennas: considerations for surface-enhanced spectroscopies. *ACS Photonics* **2014**, *1*, 524.

DOI: 10.1021/acsphotonics.6b00944
ACS Photonics 2017, 4, 873−883

(31) Carletti, L.; Locatelli, A.; Neshev, D.; De Angelis, C. Shaping the Radiation Pattern of Second-Harmonic Generation from AlGaAs Dielectric Nanoantennas. *ACS Photonics* **2016**, *3* (8), 1500−1507.
(32) Gutruf, P.; Zou, C.; Withayachumnankul, W.; Bhaskaran, M.; Sriram, S.; Fumeaux, C. Mechanically Tunable Dielectric Resonator Metasurfaces at Visible Frequencies. *ACS Nano* **2016**, *10*, 133.
(33) Khorasaninejad, M.; Chen, W. T.; Devlin, R. C.; Oh, J.; Zhu, A. Y.; Capasso, F. Metalenses at visible wavelengths: Diffraction-limited focusing and subwavelength resolution imaging. *Science* **2016**, *352*, 1190.
(34) Zou, C.; Gutruf, P.; Withayachumnankul, W.; Zou, L.; Bhaskaran, M.; Sriram, S.; Fumeaux, C. Nanoscale TiO_2 dielectric resonator absorbers. *Opt. Lett.* **2016**, *41* (15), 3391−3394.
(35) Lalanne, P.; Astilean, S.; Chavel, P.; Cambril, E.; Launois, H. Design and fabrication of blazed binary diffractive elements with sampling periods smaller than the structural cutoff. *J. Opt. Soc. Am. A* **1999**, *16* (5), 1143−1156.
(36) Philipp, H. R.; Taft, E. A. Optical constants of germanium in the region 1 to 10 eV. *Phys. Rev.* **1959**, *113*, 1002.
(37) Philipp, H. R.; Taft, E. A. Optical constants of silicon in the region 1 to 10 eV. *Phys. Rev.* **1960**, *120*, 37.
(38) Kallel, H.; Arbouet, A.; BenAssayag, G.; Chehaidar, A.; Potié, A.; Salem, B.; Baron, T.; Paillard, V. Tunable enhancement of light absorption and scattering in $Si_{1-x}Ge_x$ nanowires. *Phys. Rev. B: Condens. Matter Mater. Phys.* **2012**, *86*, 085318.
(39) Kallel, H.; Chehaidar, A.; Arbouet, A.; Paillard, V. Enhanced absorption of solar light in Ge/Si core-sheath nanowires compared to Si/Ge core-sheath and $Si_{1-x}Ge_x$ nanowires: A theoretical study. *J. Appl. Phys.* **2013**, *114*, 224312.
(40) Naffouti, M.; David, T.; Benkouider, A.; Favre, L.; Cabie, M.; Ronda, A.; Berbezier, I.; Abbarchi, M. Fabrication of core−shell nanostructures via silicon on insulator dewetting and germanium condensation: towards a strain tuning method for SiGe-based heterostructures in a three-dimensional geometry. *Nanotechnology* **2016**, *27*, 305602.
(41) Celebrano, M.; Baselli, M.; Bollani, M.; Frigerio, J.; Shehata, A. B.; Frera, A. D.; Tosi, A.; Farina, A.; Pezzoli, F.; Osmond, J.; Wu, X.; Hecht, B.; Sordan, R.; Chrastina, D.; Isella, G.; Duo, L.; Finazzi, M.; Biagioni, P. Emission engineering in germanium nanoresonators. *ACS Photonics* **2015**, *2* (1), 53−59.
(42) Gómez-Medina, R.; García-Cámara, B.; Suárez-Lacalle, I.; González; Moreno, F.; Nieto-Vesperinas, M.; Sáenz, J. J. Electric and magnetic dipolar response of germanium nanospheres: interference effects, scattering anisotropy, and optical forces. *J. Nanophotonics* **2011**, *5*, 053512.
(43) Wakayama, Y.; Tagami, T.; Shun-Ichiro, T. Formation of Si islands from amorphous thin films upon thermal annealing. *J. Appl. Phys.* **1999**, *85* (12), 8492.
(44) Korzec, M. D.; Wagner, B.; Roczen, M.; Rech, B.; Schade, M. Equilibrium shapes of poly-crystalline silicon nanodots. *J. Appl. Phys.* **2014**, *115*, 074304.
(45) Wakayama, Y.; Tagami, T.; Shun-Ichiro, T. Three-dimensional islands of Si and Ge formed on SiO2 through crystallization and agglomeration from amorphous thin films. *Thin Solid Films* **1999**, *350* (1), 300−307.
(46) Humlíček, J.; Garriga, M.; Alonso, M. I.; Cardona, M. Optical spectra of SixGe1− x alloys. *J. Appl. Phys.* **1989**, *65* (7), 2827−2832.
(47) Ahuja, R.; Persson, C.; Da Silva, A. F.; De Almeida, J. S.; Araujo, C. M.; Johansson, B. Optical properties of SiGe alloys. *J. Appl. Phys.* **2003**, *93* (7), 3832−3836.
(48) Bahng, J. H.; Kim, K. J.; Ihm, S. H.; Kim, J. Y.; Park, H. L. Evolution of optical constants and electronic structure of disordered Si1-xGex alloys. *J. Phys.: Condens. Matter* **2001**, *13* (4), 777.
(49) Sutter, E.; Sutter, P. Assembly of Ge nanocrystals on SiO2 via a stress-induced dewetting process. *Nanotechnology* **2006**, *17*, 3724.
(50) Zhang, P.; Yang, B.; Rugheimer, P.; Roberts, M.; Savage, D.; Liu, F.; Lagally, M. Influence of germanium on thermal dewetting and agglomeration of the silicon template layer in thin silicon-on-insulator. *J. Phys. D: Appl. Phys.* **2009**, *42*, 175309.
(51) Vynck, K.; Burresi, M.; Riboli, F.; Wiersma, D. S. Photon management in two-dimensional disordered media. *Nat. Mater.* **2012**, *11*, 1017.
(52) Van Lare, M.-C.; Polman, A. Optimized Scattering Power Spectral Density of Photovoltaic Light-Trapping Patterns. *ACS Photonics* **2015**, *2*, 822.
(53) Sapienza, R.; Thyrrestrup, H.; Stobbe, S.; Garcia, P. D.; Smolka, S.; Lodahl, P. Cavity Quantum Electrodynamics with Anderson-Localized Modes. *Science* **2010**, *327*, 1352.
(54) Strudley, T.; Zehender, T.; Blejean, C.; Bakkers, E. P.; Muskens, O. L. Mesoscopic light transport by very strong collective multiple scattering in nanowire mats. *Nat. Photonics* **2013**, *7*, 413.
(55) Wiersma, D. S. Disordered photonics. *Nat. Photonics* **2013**, *7*, 188.
(56) Riboli, F.; Caselli, N.; Vignolini, S.; Intonti, F.; Vynck, K.; Barthelemy, P.; Gerardino, A.; Balet, L.; Li, L. H.; Fiore, A.; Gurioli, M.; Wiersma, D. S. Engineering of light confinement in strongly scattering disordered media. *Nat. Mater.* **2014**, *13* (7), 720.
(57) Kuznetsov, A. I.; Miroshnichenko, A. E.; Fu, Y. H.; Zhang, J.; Luk'yanchuk, B. Magnetic light. *Sci. Rep.* **2012**, *2*, 492.

DOI: 10.1021/acsphotonics.6b00944
ACS Photonics 2017, 4, 873−883

Supporting Information

Manuscript title: All-Dielectric colour filters using SiGe-based Mie resonator arrays

Authors: Thomas Wood, Meher Naffouti, Johann Berthelot, Thomas David, Jean-Benoît Claude, Léo Métayer, Anne Delobbe, Luc Favre, Antoine Ronda, Isabelle Berbezier, Nicolas Bonod and Marco Abbarchi

3 pages

Fig S1 Supplementary simulations to show agreement with measured data for sample A.

Fig S2 (a) Refractive index n and (b) extinction coefficient k of pure Si and Ge, and a binary mix containing 20% Ge

Fig S3 (a) Full (including non-templated regions) bright-field optical microscopy image of the reflected colours observed on arrays r1-r9 on sample A. (b) SEM image of a spontaneously dewetted region of sample A. (c) Optical microscopy image of sample B. (d) Comparison of measured reflectance on spontaneously dewetted regions of samples A and B and calculated reflectance for bare, polished silicon. (e) Scattered light spectra from spontaneously dewetted regions on samples A and B

FDTD Simulations

The simulations presented were carried out using a home-made FDTD (Finite Difference Time Domain) code, written in C++. The objects in the simulation space were discretized onto a 3D grid of 10nm resolution, with the resonators placed within a high accuracy region with twice the spatial resolution. The overall dimensions of the simulation region were P×P×0.5µm (in x, y and z respectively), where P is the array periodicity in the substrate plane. The simulation space, in which the substrate occupied the <xy> plane used periodic boundary conditions on the x and y extrema, and absorbing boundary conditions in z. In the reflection configuration, light was injected using a broadband plane wave source at normal incidence on the substrate, and the reflection coefficients were obtained using a Poynting vector surface monitor covering the full <xy> plane above the substrate and resonator. The plane wave injected was polarized such that the electric field was oriented along the x axis and the magnetic field along the y axis. The near field distributions were collected by frequency domain monitors in the <xz> plane (electric field) and <yz> plane (magnetic field). In the diffusion configuration, electric dipoles were placed at three different spatial positions (determined at random) inside the resonators in the three orthogonal polarisations x,y,z (nine dipoles in total). The electromagnetic energy radiated from the resonators was collected by a Poynting monitor box covering the upper half plane (above the substrate), with incoherent summing of energy from each of the nine dipoles. The array periodicity P for the diffusion simulations was fixed at 450nm, a value deemed large enough to prevent coupling of fields in neighbouring resonators. The refractive indices used for the materials were $n_{Si/SiGe,sim}$ = 4, $n_{SiO_2,sim}$ = 1.5, $k_{Si/SiGe/SiO_2,sim}$ = 0 (see the supplemental information for more details on how the refractive index of SiGe was estimated).

In order to demonstrate the ability of the FDTD simulations to accurately predict the optical properties of the MR filter arrays, the true island radii measured from the SEM images have been incorporated into the calculations. The simulated reflectance spectra reported in the supplemental material Fig S1 for selected arrays on sample A (r6 – r9). Discrepancies with the measured data shown in Fig 6 (a) include a blue shifting of the simulated spectral positions of the pass-bands (and resonances). This could be attributed to the change in refractive index – and therefore the optical volume – of the resonators upon addition of Ge that is only approximated in the simulations ($n_{SiGe,sim}$=4, see detailed discussion below). If the true refractive index of the SiGe was higher than the value of 4 used in the simulations, we would indeed observe higher experimentally measured resonant wavelengths. Furthermore, in the simulations the resonators are all identical, whereas in reality a small size dispersion is seen from the SEM measurements. The effect of this dispersion is to "blur" the minima of reflected intensity and so broaden the FWHM of the pass-bands from near 50nm in the simulations to approximately 100nm in the measured data, whilst at the same time reducing the depth of the measured pass-band minima. Furthermore, the spectral features at short wavelengths (λ<450nm)

are not visible in the measured data. This can be attributed to the strong absorption in the SiGe material that is not accounted for in the simulations ($k_{SiGe,sim}$=0).

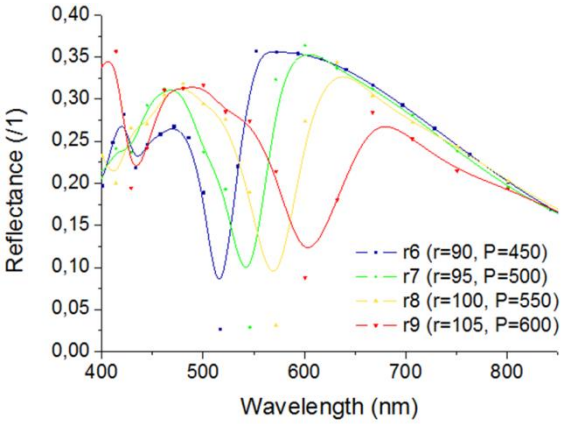

Fig S1 Supplementary simulations to show agreement with measured data for sample A. r is the island radius, P the array periodicity (units in the legend are nm).

Refractive index of SiGe

The complex refractive indices of Si and Ge and the theoretical refractive index of a binary mixture containing 20% Ge, i.e. with stoichiometry $Si_{0.8}Ge_{0.2}$, are shown in Fig S2. It can be seen that the imaginary component of the refractive index of Ge is orders of magnitude higher than for Si over a large part of the visible spectral region, explaining the need to reduce the concentration of Ge in SiGe alloys if nanostructures displaying low absorption are to be obtained.

For the purposes of the simulations, the constant (wavelength independent) value of the refractive index of the $Si_{0.8}Ge_{0.2}$ alloy was approximated as 4, this being the value in the centre of the considered spectral region, i.e. at 600nm. The imaginary refractive index k was considered negligible, in part justified by the high percentage of low-absorbance Si in the alloy. Furthermore, as can be seen from the agreement between the measured data in Fig 6 (a) and Fig S1, the neglecting of absorption in the SiGe islands is not a limiting factor in the accuracy of the simulations.

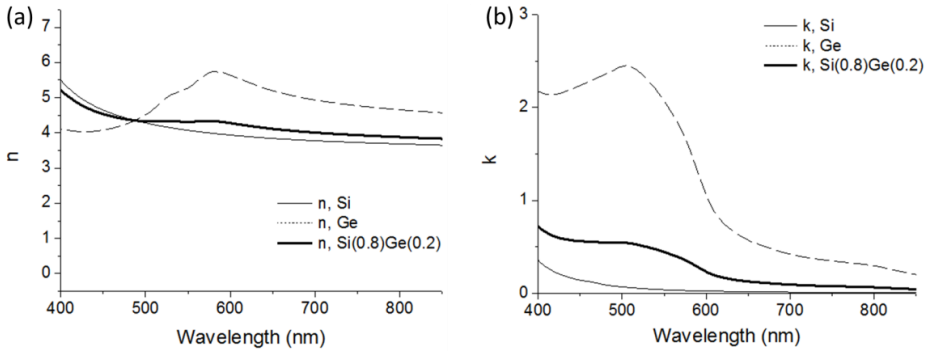

Fig S2 (a) Refractive index n and (b) extinction coefficient k of pure Si and Ge, and a binary mix containing 20% Ge.

Spontaneously dewetted regions

We examined the anti-reflective properties of the spontaneously dewetted regions of the samples found surrounding the arrays templated by LMIS-FIB milling, shown in Fig S3 (a,c). The electron microscopy image in Fig S3 (b) shows that the SiGe islands formed outside the templated regions of sample A vary greatly in size, from several tens up to several hundreds of nanometers in radius. As discussed in the manuscript, the dimensions of the particles determine the range of wavelengths of

light with which they will interact most efficiently, and so high size dispersion yields a broadband light-matter interaction. This can be seen from the black appearance of the spontaneously dewetted regions on sample A in Fig S3 (a) and quantified by the reflectance measurements shown in Fig S3 (d), which also features the reflectance of bare silicon for reference. It can be seen that a reduction of over 60% in the reflected intensity is attained over the full visible spectral region on the spontaneously dewetted regions of sample A. This observation carries significant importance for applications where spectral selectivity is not required and a broadband anti-reflective behaviour is needed, such as photovoltaics or sensing.

In the case of sample B, as seen in Fig S3 (c), the spontaneously dewetted area presents an orange-red hue, similar in colour to that of pixel r9. Fig S3 (d) shows that the reflectance is higher than for the spontaneously dewetted region of sample A over most of the visible spectral range. We can therefore infer that the average size of particles produced by spontaneously dewetting the thicker SiGe layer found on sample B is close to the size of particles obtained by template-assisted-dewetting in array r9 on the same sample. Furthermore, due to the homogeneous colour observed we conclude that the particle size distribution is relatively tight, making such a system unsuitable for broadband anti-reflective applications. We note also that the overall structure of the system is not optimised for anti-reflection purposes, and that decreasing the BOX layer thickness would lead to improved light trapping.

Finally, we consider the scattering spectra of the spontaneously dewetted regions on samples A and B shown in Fig S3 (e), which have been normalised using the maximum scattered intensities obtained for array r7 on sample A and r8 on sample B. These arrays are those with the highest periodicities characterised on each sample, and so the islands they contain present the largest number of resonances. They therefore have the optical properties nearest to the spontaneously dewetted areas, where the broad scattering spectra are owed to the high size dispersion of islands, explaining why they were chosen to normalise this data. Fig S3 (e) shows quantitatively that the overall scattered intensity on the spontaneously dewetted areas is much lower than for the templated regions, which is confirmed visually by the “dimmer” appearance of the former in the optical images shown in the inset. Furthermore, Fig S3 (e) shows that the spectral distribution of light for the spontaneously dewetted regions is, as expected due to the disorder, much greater than for the scattering spectra of Fig 5 (a) and (c) where distinct peaks are observed.

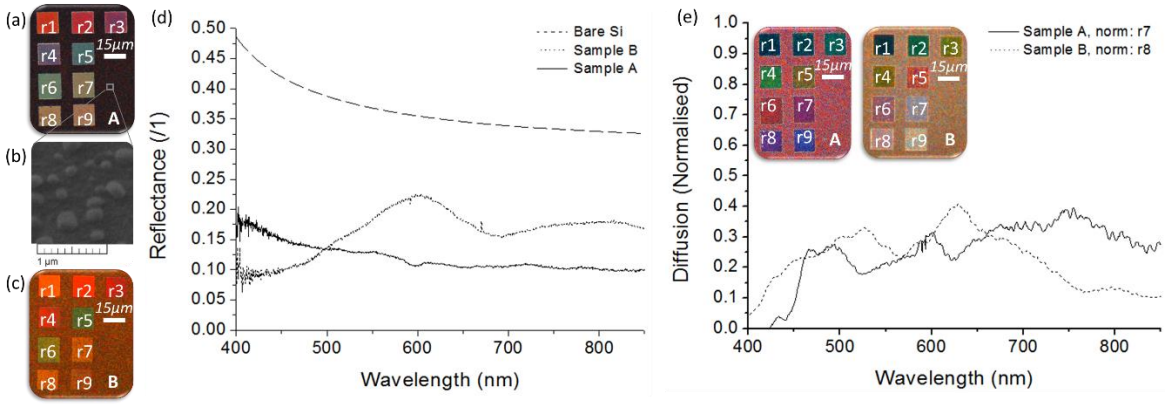

Fig S3 (a) Full (including non-templated regions) bright-field optical microscopy image of the reflected colours observed on arrays r1-r9 on sample A. (b) SEM image of a spontaneously dewetted region of sample A. (c) Full bright-field optical microscopy image of sample B. (d) Comparison of measured reflectance on spontaneously dewetted regions of samples A and B and calculated reflectance for bare, polished silicon. (e) Scattered light spectra from spontaneously dewetted regions on samples A and B, normalised using the maximum scattering intensity of the array with the largest periodicity characterised on that sample (i.e. r7 for sample A and r8 for sample B). Inset: dark-field optical microscopy images of samples A and B.